Low Boom Configuration Analysis with FUN3D Adjoint Simulation Framework

Michael A. Park*

Off-body pressure, forces, and moments for the Gulfstream Low Boom Model are computed with a Reynolds Averaged Navier Stokes solver coupled with the Spalart-Allmaras (SA) turbulence model. This is the first application of viscous output-based adaptation to reduce estimated discretization errors in off-body pressure for a wing body configuration. The output adaptation approach is compared to an *a priori* grid adaptation technique designed to resolve the signature on the centerline by stretching and aligning the grid to the freestream Mach angle. The output-based approach produced good predictions of centerline and off-centerline measurements. Eddy viscosity predicted by the SA turbulence model increased significantly with grid adaptation. Computed lift as a function of drag compares well with wind tunnel measurements for positive lift, but predicted lift, drag, and pitching moment as a function of angle of attack has significant differences from the measured data. The sensitivity of longitudinal forces and moment to grid refinement is much smaller than the differences between the computed and measured data.

I. Introduction

A detailed review of the history and state-of-the-art of sonic boom modeling is provided by Plotkin[1] and literature surveys are provided by Ozcer[2] and Park.[3] Advancements in Computational Fluid Dynamics (CFD) tools and their application have resulted in significant improvements to near-field sonic boom signature prediction. Methods have been developed to align initial grids with the Mach cone before beginning analysis.[4] Hybrid methods have been developed[5–7] where near-body unstructured grid solutions are interpolated to shock-aligned structured grid methods to increase accuracy. Solution adaptive grid methods[8,9] have been employed to improve the accuracy of unstructured grid methods for long propagation distances. Output-adaptive approaches have been applied to sonic boom prediction in two-dimensions (2D) with a discontinuous Galerkin method,[10,11] a three-dimensional (3D) Cartesian grid method,[12] and 3D unstructured grid methods.[13–15]

When CFD validation studies have been performed on complex geometries, the existing methods perform much better for the forward portion of the signature than the aft portion.[4,14] A notable exception is Signature 47 of the Shaped Sonic Boom Demonstrator (SSBD) program.[16] There are many sources of uncertainty in simulation and measurements of off-body pressure signatures. Wind tunnel test sections can exhibit pressure fluctuations on the same order as the signature.[17–19] Some of the uncertainty in the prediction of the aft signature may be due to uncertainties in the geometry.[3]

Often, near-field sonic boom predictions are performed with Euler methods, so the effect of a viscous boundary layer is absent. Output adaptive Euler and turbulent Reynolds Averaged Navier-Stokes (RANS) approaches were applied to predict extremely near-field pressure signatures of a plume in supersonic flow.[20] Differences in signatures between Euler and RANS simulations motivated the use of RANS coupled with a turbulence model for the prediction of off-body pressure signatures of a more complex wing body configuration.

A low boom configuration must also have good aerodynamic performance to be a practical design. Improvements in aerodynamic performance can result in reductions in fuel required to perform a mission. A reduction in fuel usage also reduces empty vehicle weight, vehicle volume, and environmental impact. Reducing the weight and volume of the aircraft directly aids in sonic boom mitigation.[21] Therefore, accurate

*Research Scientist, Computational AeroSciences Branch, NASA Langley Research Center, MS 128, Hampton, VA 23681, AIAA Senior Member.

predictions of lift, drag, and pitching moment are important to the design of a practical aircraft and are included in this study.

II. FUN3D Flow Solver

This study utilizes the Fully Unstructured Navier-Stokes Three-Dimensional (FUN3D) simulation framework. FUN3D is a suite of tools for the analysis and design of a wide range of aerospace vehicles. The user manual, an extensive list of references, and example applications are available at the FUN3D website.[†] The FUN3D framework contains multiple algorithms to allow for the evaluation and comparison of different numerical methods. The following FUN3D description is limited to the methods utilized in this study. A finite-volume method[22] is applied to tetrahedral grids. The flow variables are stored at the vertexes or nodes of the mesh. At interfaces delimiting neighboring median dual control volumes, the inviscid fluxes are computed using Roe[23] or van Leer[24] approximate Riemann solvers based on the values on either side of the interface. For second-order accuracy, interface values are obtained by extrapolation of the control volume centroidal values, based on gradients computed at the mesh vertexes using an unweighted least-squares technique.[22] The reconstruction limiter is based on the framework of Barth and Jespersen,[25] but the min and max functions are replaced with a differentiable function.[26] This limiter, denoted `hvanalbada`, is frozen[27] after 1000 iterations.

The full viscous fluxes are discretized using a finite-volume formulation in which the required velocity gradients on the median dual faces are computed using the Green-Gauss theorem. The solution at each time-step is updated with a backward Euler time-integration scheme. At each time step, the linear system of equations is approximately solved with a point-implicit procedure.[28] Local time-step scaling is employed to accelerate convergence to steady state. The Spalart-Allmaras (SA) model[29] is used to model turbulence.

III. Output-Based Adaptation

Output-based adaptation requires the solution of discrete adjoint equations.[3,30,31] These linear adjoint equations are solved with a time-marching method that produces the same asymptotic convergence rate as the flow equations.[28] To improve adjoint iterative convergence, a generalized conjugate residual (GCR) scheme[32] is used with the standard point-implicit procedure as search directions. The linearization of the turbulence model and eddy viscosity is included in the adjoint residual. The reconstruction limiter is frozen, which removes its dependency from the adjoint linearization.

Venditti[33] described an output-based error estimation and adaptation scheme which utilizes an embedded grid. This has been implemented in 3D[34] within a parallel[35] framework. The embedded grid required for the Venditti error estimator can be prohibitively large (eight times the original grid) for 3D problems, which effectively limits the problem size of the output adaptive method. A single-grid error estimation procedure has been described[3] that produces similar adaptation guidance as the embedded-grid procedure for Euler[3] and turbulent[36] flows.

Venditti[33] provided a procedure to calculate a new grid spacing request from the adaptive indicator and a user specified error tolerance. In this study, this error tolerance is set to half the total remaining error estimate for each adaptation. The anisotropy of mesh elements is based on a scaled Mach Hessian, where the element size in the smallest spacing direction is dictated by the output-based spacing request.[33] This scaled Hessian is expressed as a metric, which is utilized by the adaptive grid mechanics. The selection of the Mach Hessian to determine the anisotropy of the metric is arbitrary, but has produced reasonable results for problems with shocks and boundary layers.[20]

Parallel grid mechanics described by Park and Darmofal[3,37] are used to adapt the grid. The local elemental operators of node insertion, node movement, element swap, and element collapse are utilized to iteratively drive the edge lengths to unity in the specified metric. The grid adaptation mechanics suffer from robustness problems when performing highly anisotropic adaptation near curved boundaries. Also, the discretization in FUN3D is more accurate for semi-structured right-angle elements in the boundary layer.[38] To address both of these issues, the near-wall boundary layer grid is frozen during the adaptation process. This approach is not applicable to problems with initially under-resolved geometry or boundary layers because that portion of the grid is held constant during the simulation. However, this approach is a

[†] `http://fun3d.larc.nasa.gov` [accessed June 2011].

powerful technique for problems with important off-body anisotropic features, i.e., sonic boom propagation. Details of the adaptation technique with constant near-wall boundary layer grid are available in Andren and Park[39] and Park and Carlson.[20]

The cost function for the adjoint error estimation procedure is the integral of quadratic pressure deviation over a surface s in the domain,

$$f = \frac{1}{A_s} \iint_s \left(\frac{p - p_\infty}{p_\infty} \right)^2 \, \mathrm{d}s, \tag{1}$$

where A_s is the area of the integration surface. The adaptation is focused on improving the calculation of pressure near this surface also referred to as the sensor. Integrating the square of pressure deviation has been shown to produce more accurate signatures with less control volumes than integrating the pressure deviation directly.[12] In this study, a cylindrical surface, aligned to the x-axis, is defined for s to resolve the signature on and off the centerline.[14] The extent of the integration surface can be optionally restricted to the interior of a bounding box to focus on a portion of the cylinder surface.

IV. Model and Experiment Description

Two cooperative wind tunnel tests were performed by the National Aeronautics and Space Administration and the Gulfstream Aerospace Corporation. The model is designed to have a Quiet Spike$^{\mathrm{TM}}$ telescoping forward fuselage extension[40] integrated into a low boom and low drag design.[41] Separate boom and performance wind tunnel tests were performed, each with a different model support sting. The boom model is smaller than the performance model. This allows off-body pressure measurements at further relative distances from the model and performance measurements at a higher Reynolds number. The model support stings are tailored to minimize their interference on the data measured in each test.

V. Off-Body Pressure Prediction

The off-body pressure test[41] was performed in Test Section 1 of the NASA Langley Unitary Plan Wind Tunnel.[42] Test section cross section is nominally 4- by 4-feet. The wind tunnel employs sliding block nozzle, which imparts flow angularity in the test section.[42] Techniques for grit application to control boundary layer transition and guidelines for flow angularity are provided by Wassum and Hyman.[43] Grit was only used for one of the signatures presented here. The model was supported with a curved blade sting[44] that attached to the upper surface of the fuselage, Fig. 1. The wind tunnel test and simulation is performed with 3.5 million Reynolds number per foot or 0.613 million Reynolds number for the mean aerodynamic chord.

The van Leer flux function is selected for the boom propagation simulation because the Roe flux was not suitable due to the strong expansion around the blade sting. The simulations were run at Mach 1.6 and 0.25 degrees angle of attack. The wind tunnel walls are not modeled in the simulation; freestream boundary conditions are applied to the outer boundaries.

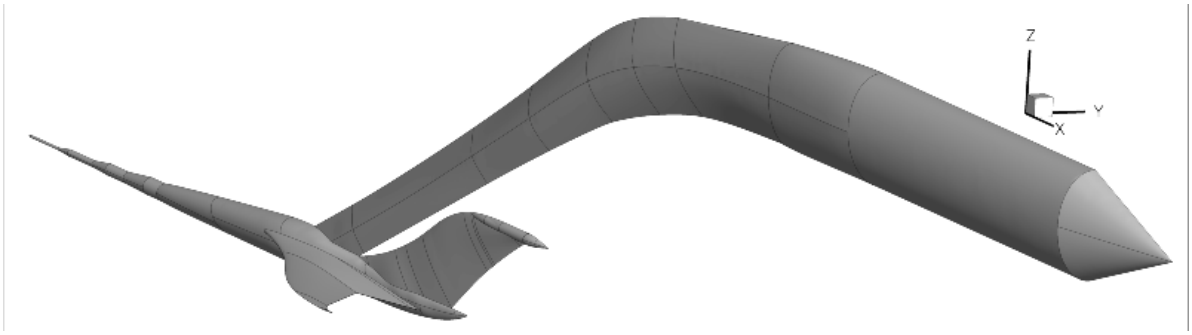

Figure 1. Boom model with blade sting.

The initial grid was generated with the VGRID and SSGRID tools.[4,45] The boundary layer grid is constant for all nodes within 0.002377 mean aerodynamic chords of the no slip boundary conditions. This corresponds to the first 12 nodes of the advancing layer mesh. The initial grid has 3.5 million nodes. Adaptation is performed eight times and the final adapted grid has 11.5 million nodes. The concatenated

convergence history of the flow solver is shown in Fig. 2 for the initial and adapted grids. The residuals of the five mean flow equations are plotted with solid lines and the residual of the SA turbulence model is plotted with a dashed line. The flow solver used 2,000 iterations on each grid. The reconstruction limiter is frozen after 1,000 iterations resulting in a rapid drop of the mean flow residuals. The adaptation mechanics interpolate the solution, which is used for each flow solver and adjoint solver restart. The mean flow equations converge approximately ten orders of magnitude on each grid and the turbulence model converges approximately nine orders of magnitude. A loosely coupled time advancement scheme is used for the SA model because it allows for guarantees on the positivity of $\tilde{\nu}$ to improve robustness during initial transients.[29] The adjoint solver utilizes 10 search directions for GCR convergence acceleration. The adjoint equations converge approximately eight orders of magnitude on each grid in 500 iterations (not shown).

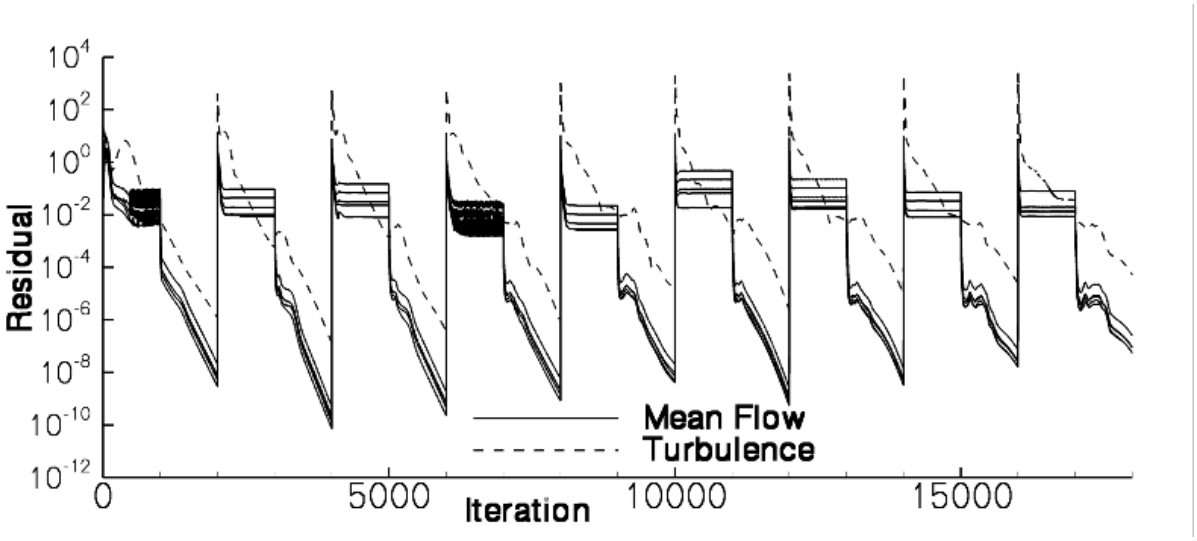

Figure 2. Concatenated convergence history of the initial and all grids adapted for off-body pressure.

The symmetry planes of the initial and adapted grids are shown in Fig. 3. The intersection of the model and the symmetry plane is shown in white. The curved blade sting is clearly seen above the fuselage and vertical tail. The initial grid is shown in the left subfigures and the adapted grid is shown in the right subfigures of Fig. 3. The normalized delta pressure $dp = (p - p_\infty)/p_\infty$ is shown in the upper subfigures. The intersection of the cylindrical boom integration surface and the symmetry plane is shown as the thick black line in Fig. 3b and Fig. 3d. The sensor cylinder s has a radius of $h/l = 2.0$, where $l = 13.2$ inches is the reference body length. Only the negative z and negative y quadrant is used. The x extent of the cylinder is $x/l = [2, 4]$. The forward limit is ahead of the bow shock. The aft limit of the integration surface was set to exclude the strong model support pressure disturbances that were not measured in the wind tunnel test. The output adaptation technique increased the grid resolution above the model to reduce the estimated error in the pressure below and to the side of the configuration, see Fig. 3b and Fig. 3d. The adapted grid upstream of the bow shock and downstream of the model is coarser. The initial grid has more high frequency content in the middle of the signature on the centerline. This difference is also observed in a close up of the symmetry plane near the model, Fig. 4.

The increase in grid resolution above the model observed in Fig. 3 is also observed in Fig. 4. The difference in the high frequency content of the middle of the signal observed in Fig. 3 is more evident in Fig. 4. The aspect ratio of the tetrahedra has been reduced and the grid is less structured in this middle region of the signature. Grid density has been increased in the wake of the configuration. The pressure aft of the configuration is smoother and the expansion at the tail has a different shape.

A closeup of the forward fuselage of the model is shown in Fig. 5. The model patch boundaries, surface grid, and surface contours are also included in Fig. 5. The delta pressure color contour range is adjusted to highlight small pressure variations behind the nose boom shocks. The nose boom shocks and expansions are targeted by the output adaptive approach above and below the model. The lower nose boom expansions are different between the initial and adapted grid. This may be due to the difference in grid orientation. The initial grid is stretched along the freestream Mach angle, but adapted grid stretching is determined by the local Mach Hessian. The current Mach Hessian recovery technique successively applies a least squares

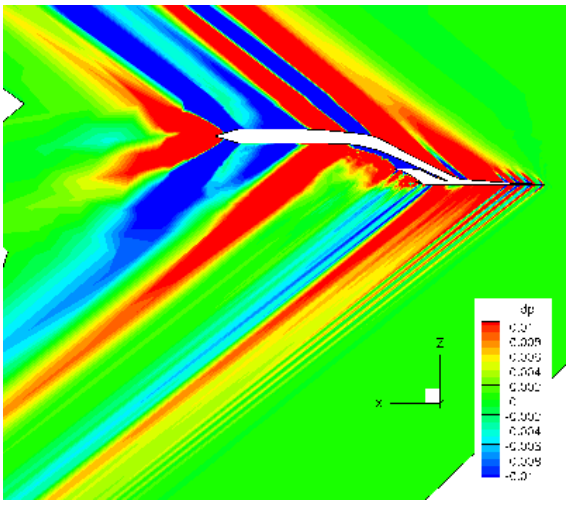

(a) Initial grid delta pressure contours.

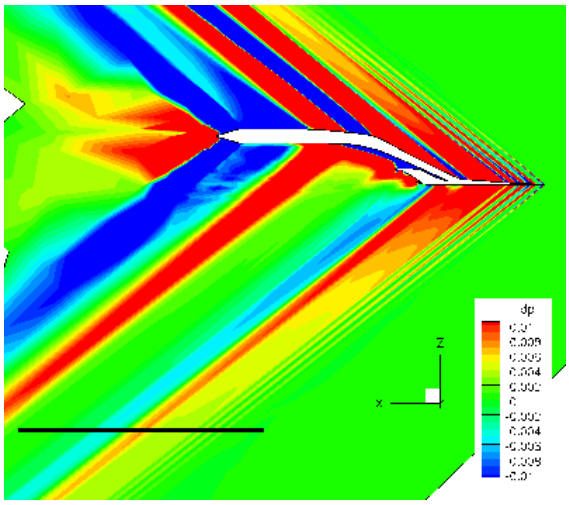

(b) Adapted grid delta pressure contours.

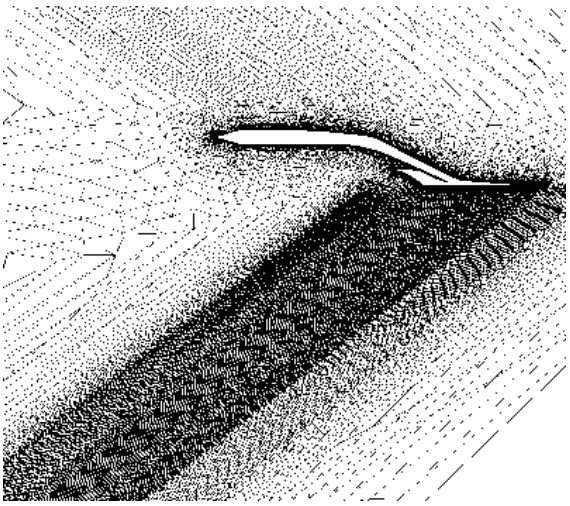

(c) Initial grid.

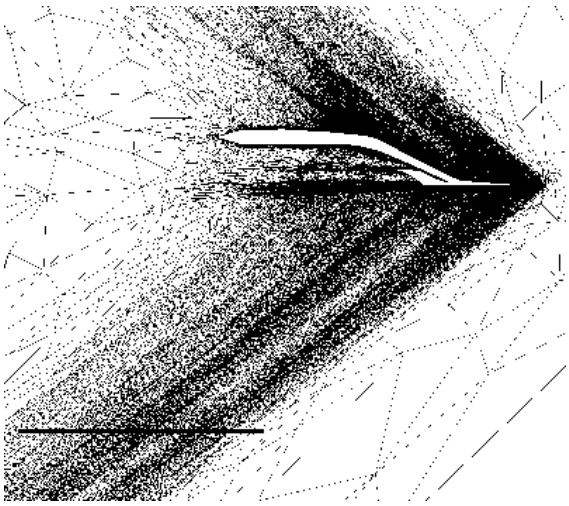

(d) Adapted grid.

Figure 3. Symmetry plane of the entire near-field boom propagation region.

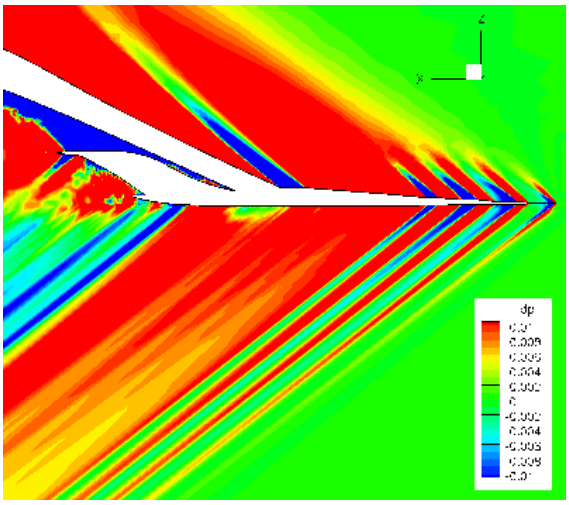

(a) Initial grid delta pressure contours.

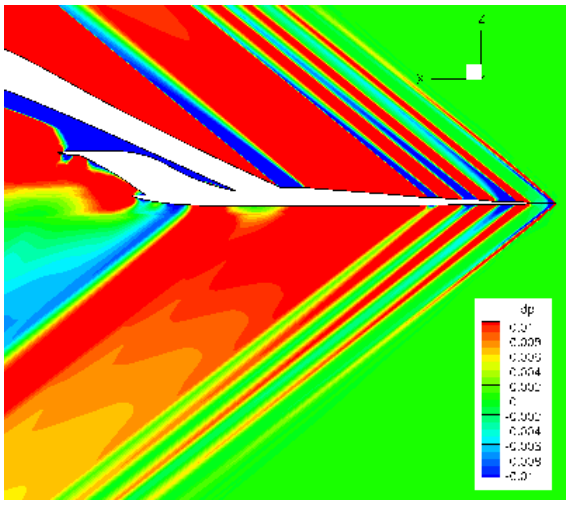

(b) Adapted grid delta pressure contours.

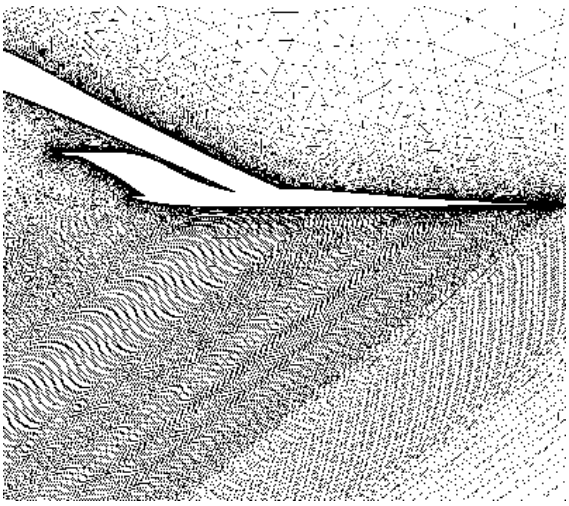

(c) Initial grid.

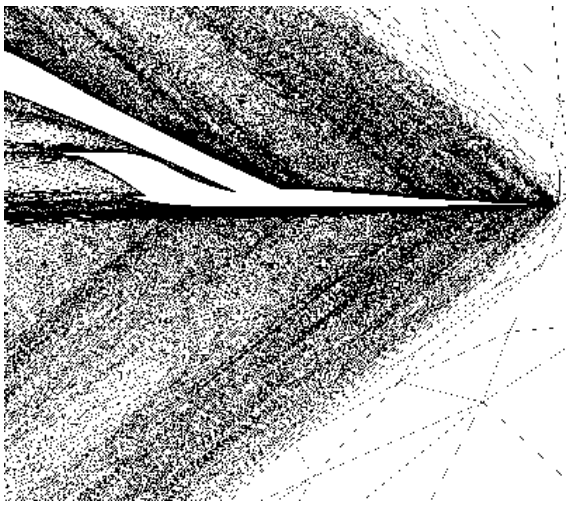

(d) Adapted grid.

Figure 4. Detailed view of the near-body propagation region symmetry plane.

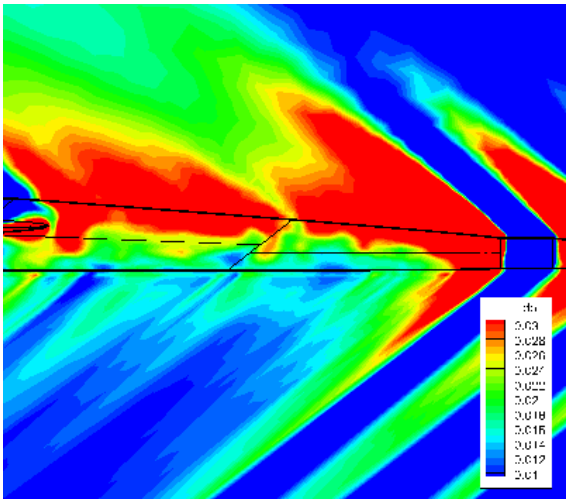

(a) Initial grid delta pressure contours.

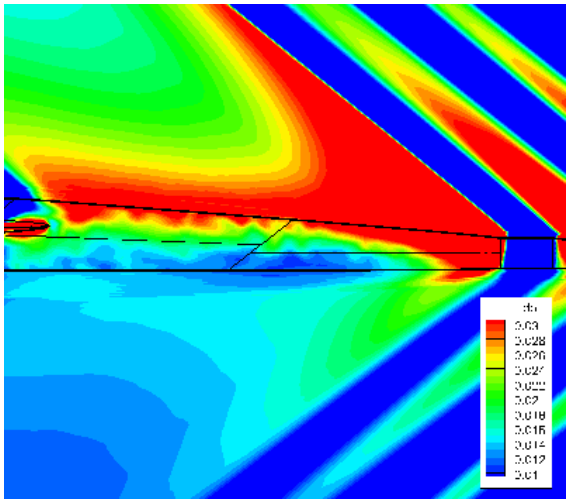

(b) Adapted grid delta pressure contours.

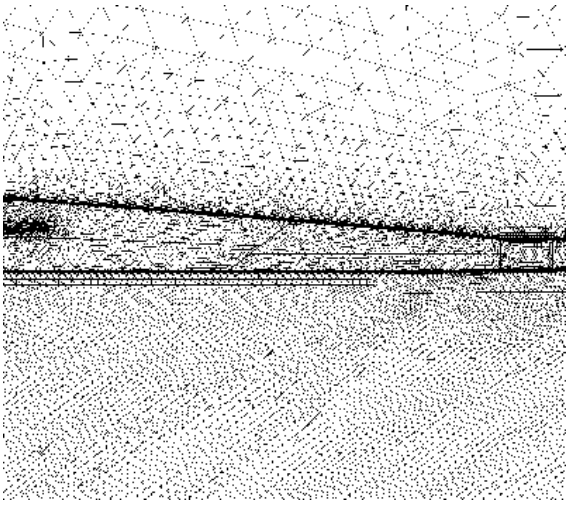

(c) Initial grid.

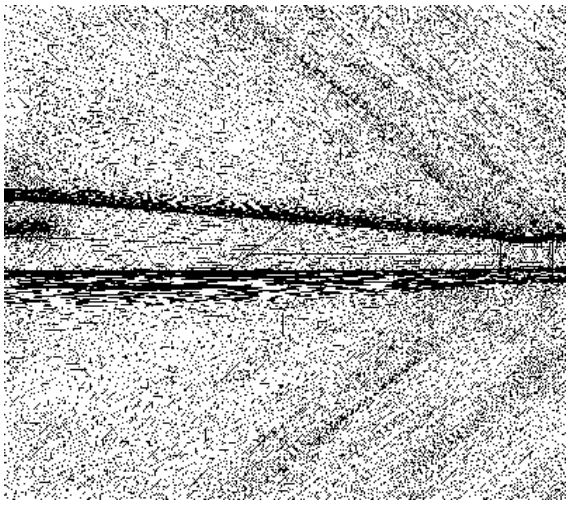

(d) Adapted grid.

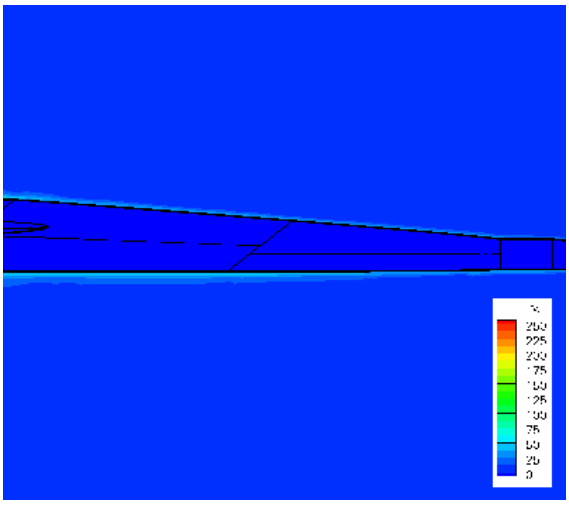

(e) Initial grid turbulence model parameter $\tilde{\nu}$.

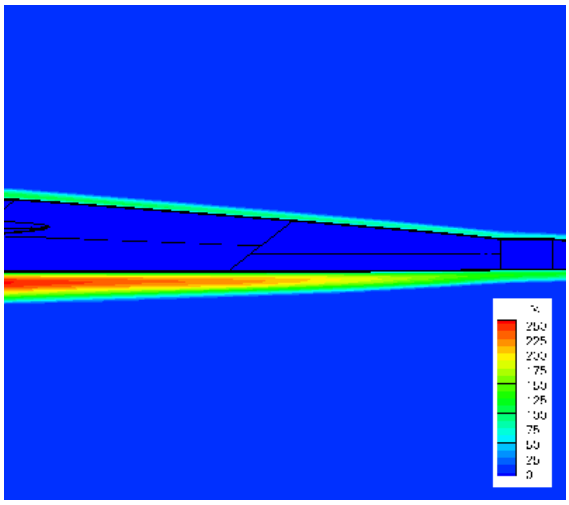

(f) Adapted grid turbulence model parameter $\tilde{\nu}$.

Figure 5. Detailed view of aft fuselage symmetry plane.

gradient technique.[22] An adaptive grid procedure that utilized a Green formulation for Hessian recovery produced better resolution of small scale details than an approach utilizing the successive least squares approach.[8]

The SA turbulence model variable $\tilde{\nu}$ is shown in the lower subfigures of Fig. 5. The region where the turbulence model is active above and below the model is well resolved by the adapted grid. The boundary layer is treated as fully turbulent. The SA turbulence model rapidly approaches the freestream value at the edge of the boundary layer. This edge region is targeted by output error estimation techniques.[46] The peak levels of the turbulence are higher for the adapted grid.

The surface pressures are uneven in both the initial and adapted grids indicating that the surface may need to be refined. The source of the high frequency disturbance in the signature propagated by initial grid is difficult to determine from the surface grid pressures. The pressures are nonsmooth at the edge of the boundary layer for both grids. It appears that the change in topology between the unsheared and sheared regions of the initial grid and the edge of the highly refined adapted boundary layer is at the same location as this nonsmoothness.

To illustrate the differences in the initial and adapted grid off centerline, a volume slice at $x/l = 0.6$ is shown in Fig. 6. The initial grid is shown on the left half of each subfigure and the adapted grid is shown on the right. The intersection of the volume grid tetrahedral elements and the plane is shown in Fig. 6(a). Pressure interpolated to the plane is shown in Fig. 6(b). Silhouettes of the wing, tail, and blade sting are seen in the center of each subfigure. The adapted grid has higher resolution in near the body and the nose boom shocks on the centerline and off the centerline. The grid has been coarsened outside of the nose shock.

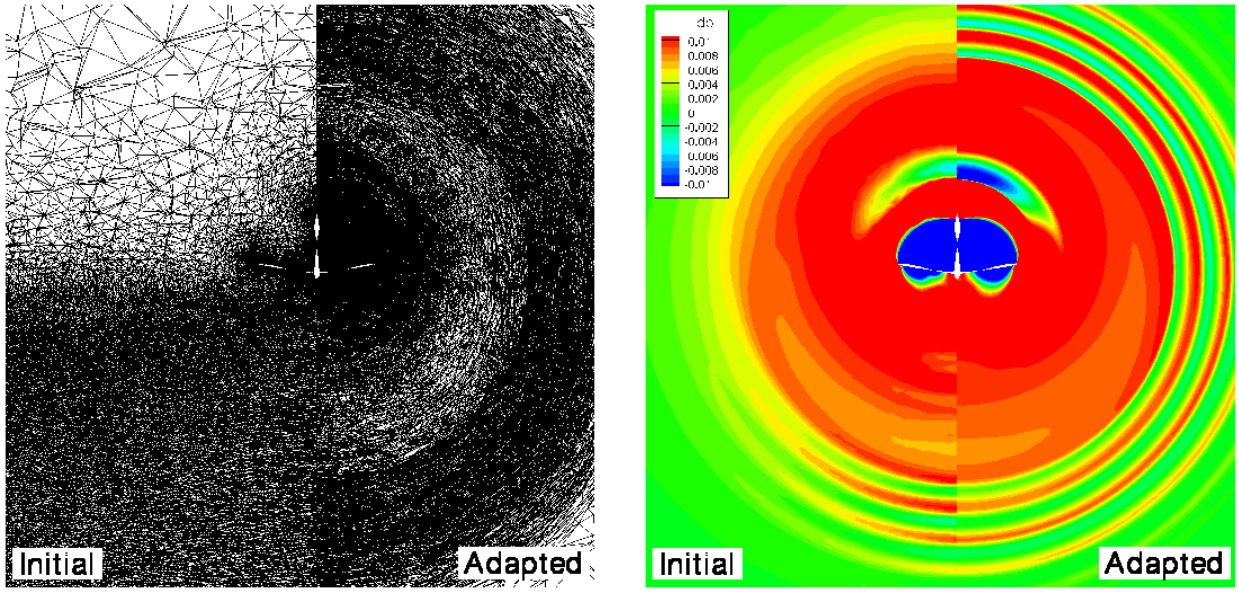

(a) Intersection of volume grid and plane.

(b) Delta pressure contours.

Figure 6. Volume slice at $x/l = 0.6$.

V.A. Pressure Signatures

The wind tunnel runs are listed in the order presented, Table 1. The distance between the pressure measurement and the x-axis is h/l. The angle between the symmetry plane and the off-track measurement location is ϕ. The measurements are made with probe 2.[41] Off track comparisons will be provided first to illustrate the most significant differences between the initial and adapted grids. Run 197 is a repeat of Run 148 with grit added to force boundary layer transition. All other Runs did not use grit and were allowed to transition naturally. All the simulations assumed a fully turbulent boundary layer without transition. The predicted signatures are shifted aft by the distance denoted in the following figure legends to align the predicted expansion in the middle of the signature to the measured location. A shift is commonly employed for wind tunnel comparisons because of slight variations in wind tunnel test section Mach number and other types of flow nonuniformity.

Table 1. NASA Langley UPWT Run descriptions in order presented.

Run	h/l	ϕ (deg)	Figure
172	1.201	26	Fig. 7a
173	1.230	38.5	Fig. 7b
174	1.338	56.5	Fig. 8a
175	1.478	81.6	Fig. 8b
156	1.730	25.5	Fig. 9a
157	1.756	35.0	Fig. 9b
158	1.829	53.4	Fig. 10a
159	2.002	83.9	Fig. 10b
140	0.49	0	Fig. 11a
133	1.2	0	Fig. 11b
148	1.7	0	Fig. 12
197[‡]	1.7	0	Fig. 12

[‡] Run 197 has grit applied to ensure boundary layer transition. All other cases are free transition.

Off centerline data for $h/l = 1.201$ and $h/l = 1.230$ is shown in Fig. 7. The series of nose boom shocks are better resolved by the adapted grid. Comparisons are made even further from the aircraft centerline in Fig. 8. The nose boom shocks predicted by the adapted grid are absent in the initial grid. The largest delta pressure is well predicted by simulations on both grids. The adapted grid predicts a similar lowest delta pressure to the initial grid near the centerline. Away from the centerline, the adapted grid has a lower delta pressure which compared well with the measured signature.

Off track delta pressure comparisons for $h/l = 1.730$ to $h/l = 2.002$ are shown in Fig. 9 and Fig. 10. The required shift increases with off track angle. A constant value of 0.0035 was added to wind tunnel measurements for Run 159, Fig. 10b, so that the delta pressure would fluctuate around a zero mean upstream of the boom shock. Reference pressure can drift before and during measurements.[47] Again at this location, the adapted grid predicts a lower delta pressure than the initial grid for the expansion, especially for the most off track location.

The predicted and measured signatures for centerline at $h/l = 0.49$ and $h/l = 1.2$ are shown in Fig. 11. Due to limitations in the model traversing mechanism at this closest location, only the aft portion of the signature was measured in Run 140, Fig. 11a. The initial grid produces high frequency signal content for $x/l = [0.8, 1.0]$ in Fig. 11a and $x/l = [1.7, 1.9]$ in Fig. 11b. The propagation of these peaks can be seen in the Fig. 3a, Fig. 4a, and Fig. 5a. The high frequencies of the aft portion of the adapted signature are also damped. The output adaptive method is resolving the signature over the entire lower cylinder quadrant and the initial grid is designed to primarily resolve the centerline.

The effect of tripping the boundary layer in the experiment is shown in Fig. 12. The approximate locations of the grit applied to the model[48] is denoted as the thick lines in Fig. 13. The open circle of Fig. 12 are the natural transition measurements and the filled squares are the measurements with grit applied. The increase in the high frequency signal at $x/l = 2.4$ in Fig. 12b coincides with the approximate location of the grit strip on the fuselage. The highest pressure measurement at $x/l = 2.6$ is closer to the predicted signatures. The low pressure region at $x/l = [2.8, 3]$ has also been affected by the change in the boundary layer state. The second low pressure valley at $x/l = 2.9$ has been increased as a result of grit application, which improves its correlation with the predicted signature. The measured peak at $x/l = 3.1$ has been reduced, which also improves the correlation with the predicted signature.

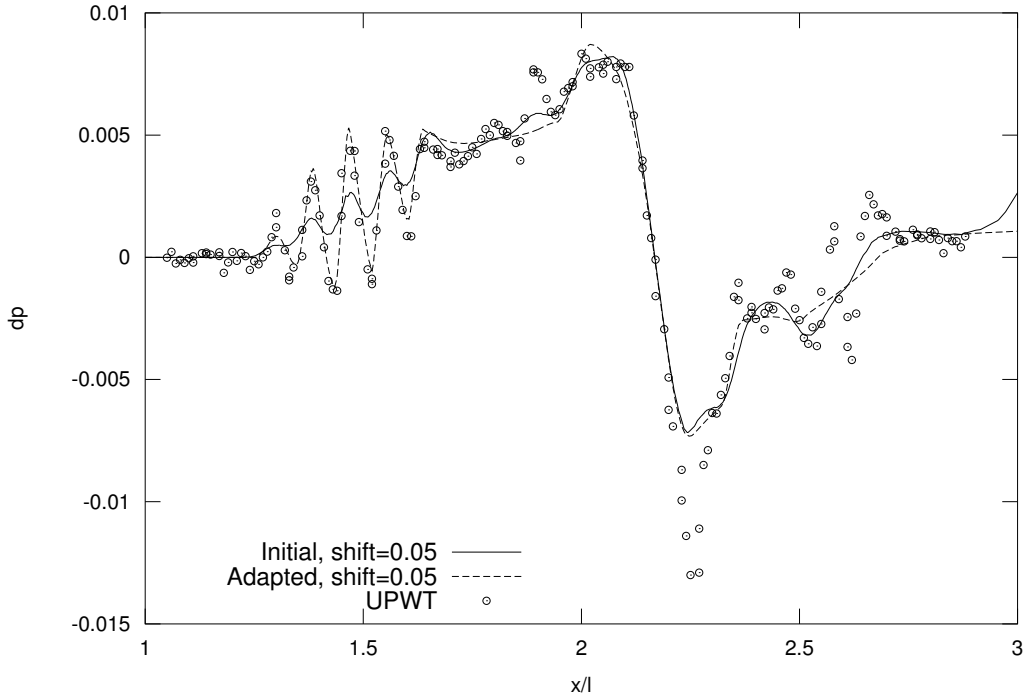

(a) Run 172, $h/l = 1.201$, $\phi = 26$.

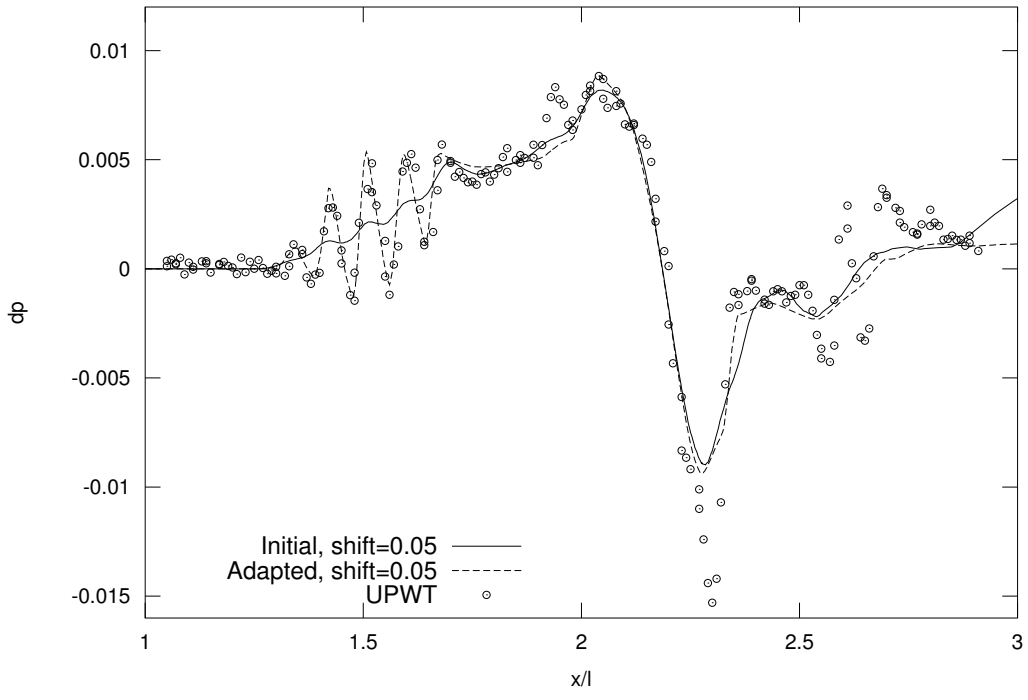

(b) Run 173, $h/l = 1.230$, $\phi = 38.5$.

Figure 7. Pressure signature slightly off centerline.

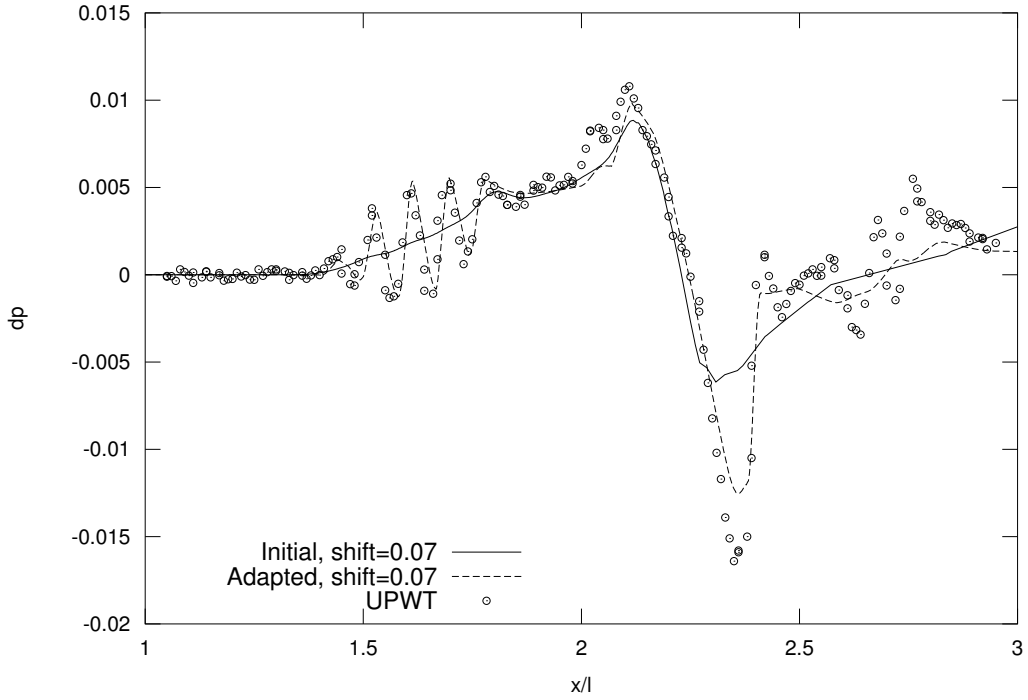

(a) Run 174, $h/l = 1.338$, $\phi = 56.5$.

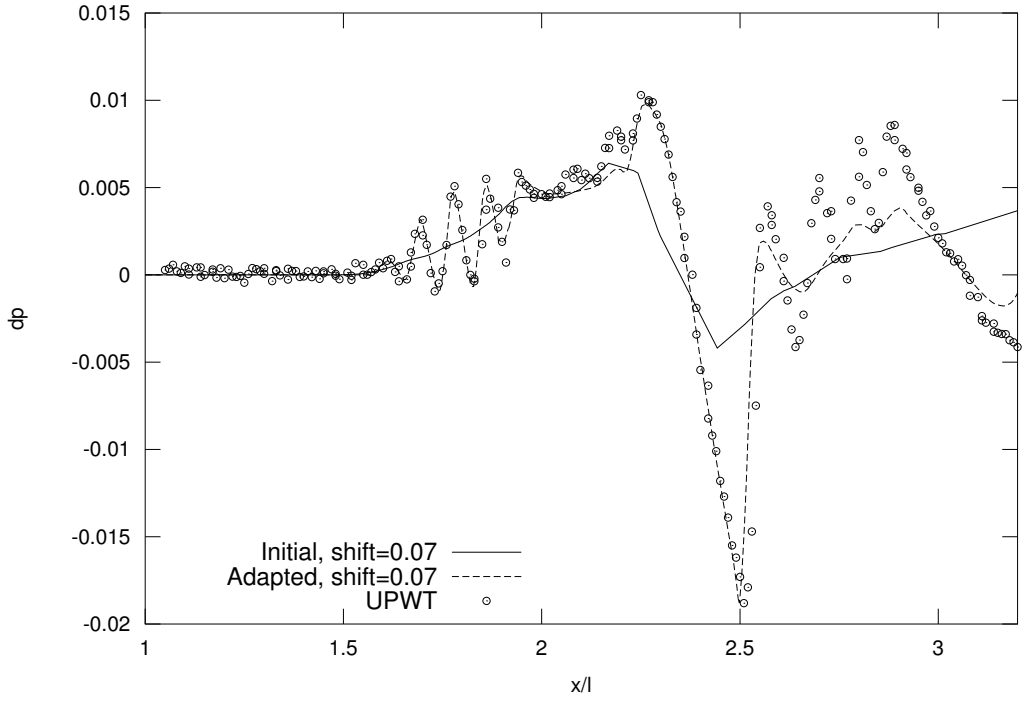

(b) Run 175, $h/l = 1.478$, $\phi = 81.6$.

Figure 8. Pressure signature far off centerline.

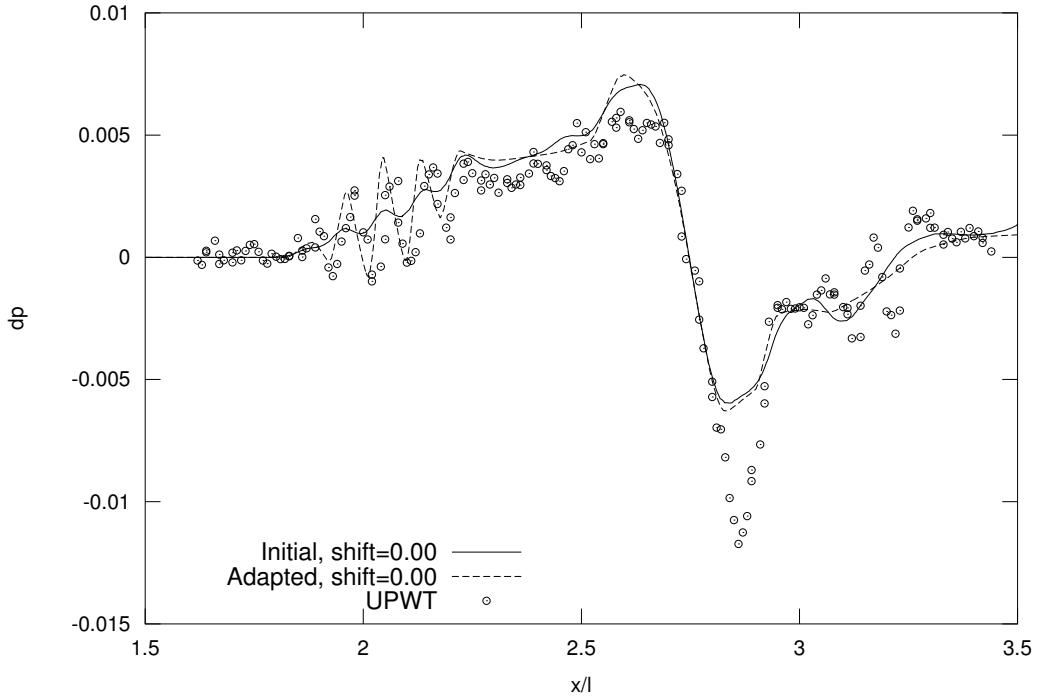

(a) Run 156, $h/l = 1.730$, $\phi = 25.5$.

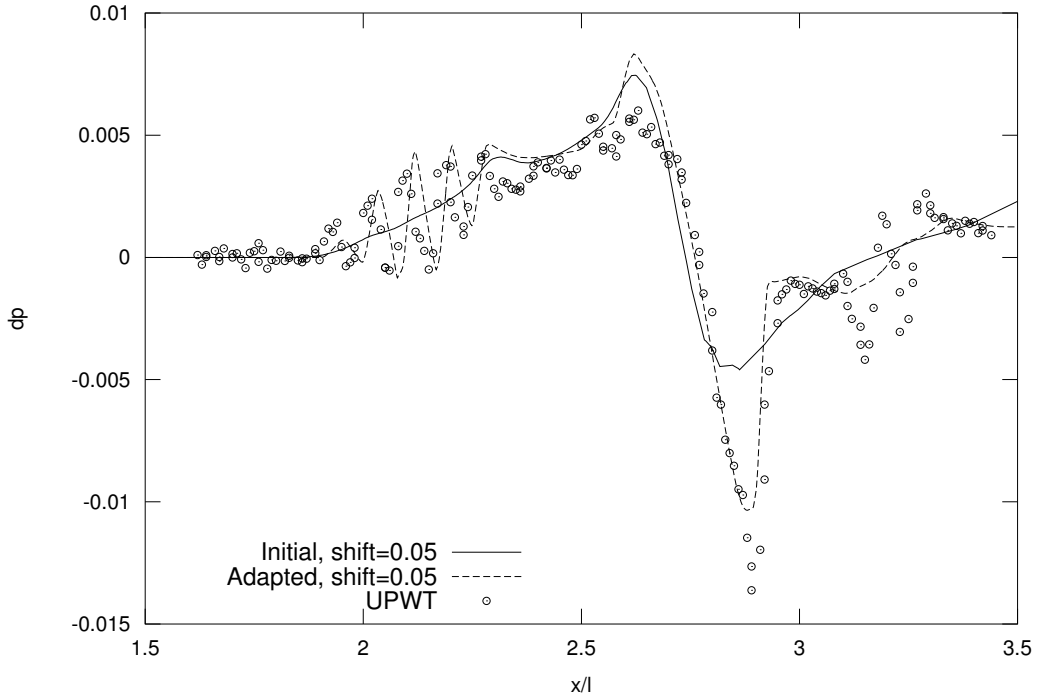

(b) Run 157, $h/l = 1.756$, $\phi = 35$.

Figure 9. Pressure signature slightly off centerline.

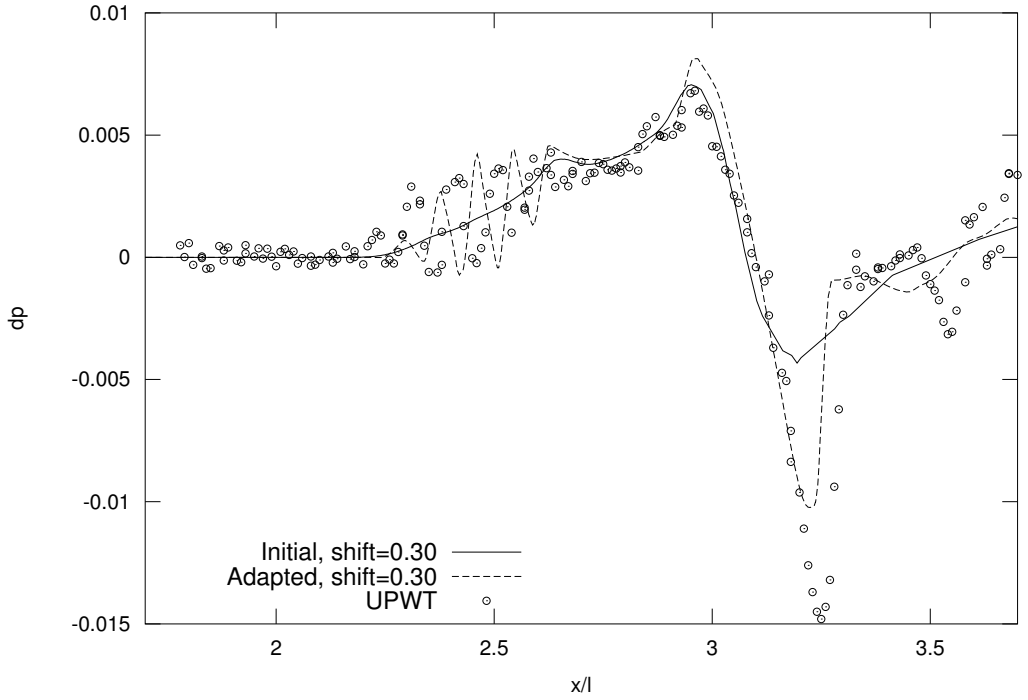

(a) Run 158, $h/l = 1.829$, $\phi = 53.4$.

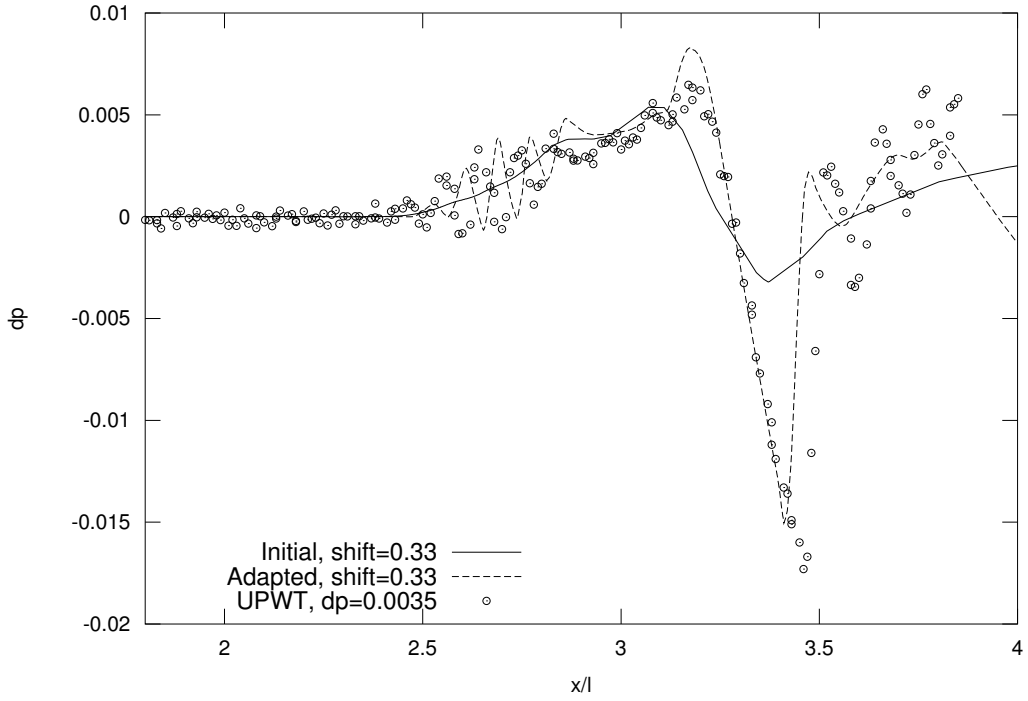

(b) Run 159, $h/l = 2.002$, $\phi = 83.9$.

Figure 10. Pressure signature far off centerline.

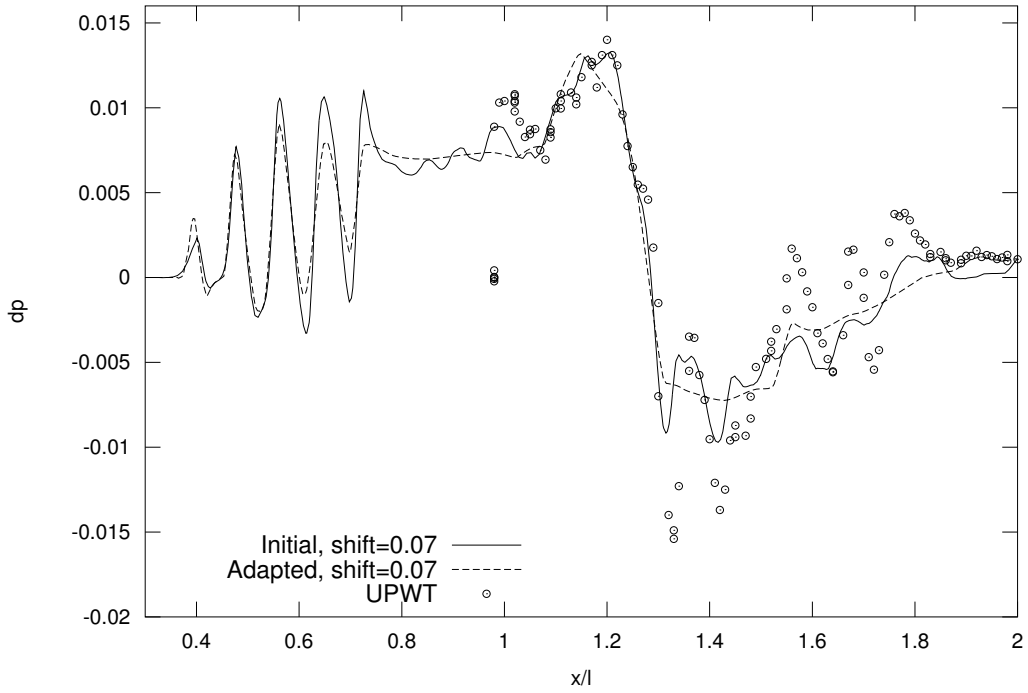

(a) Run 140, $h/l = 0.49$, $\phi = 0$.

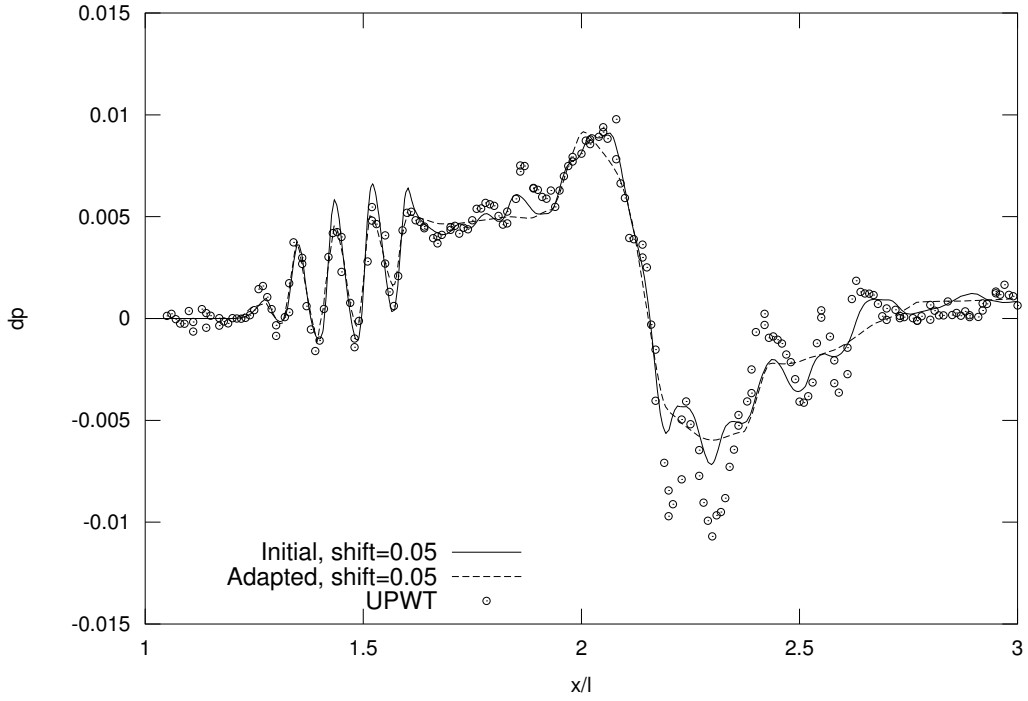

(b) Run 133, $h/l = 1.2$, $\phi = 0$.

Figure 11. Pressure signature on the centerline near the model.

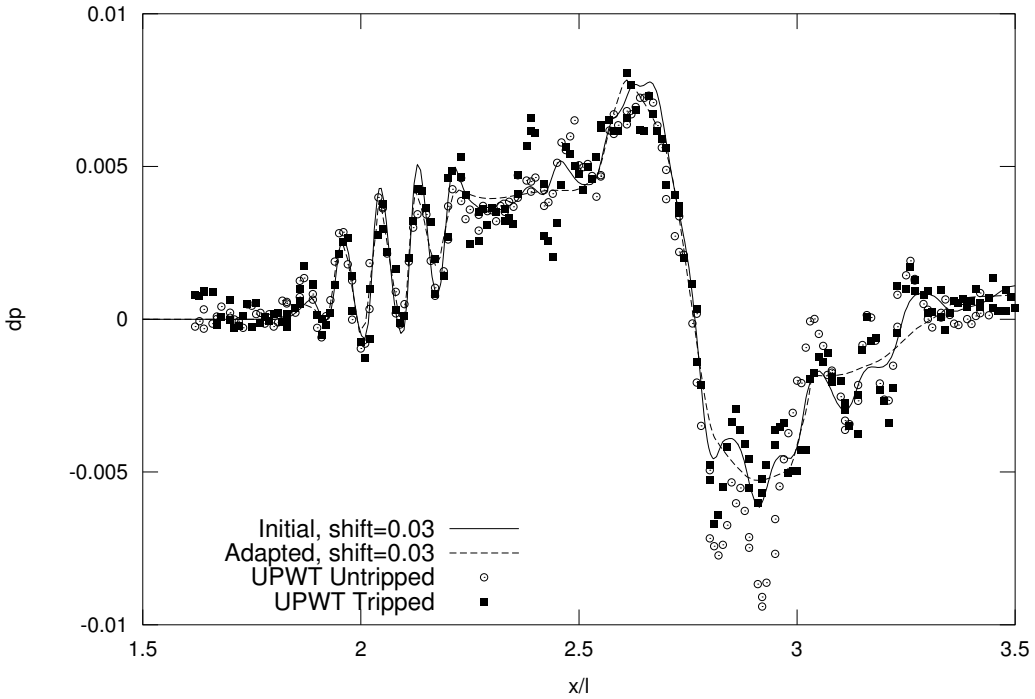

Figure 12. Pressure signature on the centerline at $h/l = 1.7$, with (Run 197) and without (Run 148) grit to trip the boundary layer in the wind tunnel.

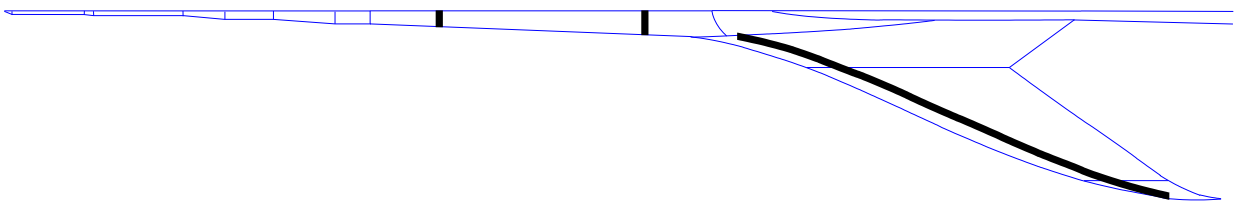

Figure 13. Planform of the model. Thick lines denote grit locations.

VI. Force and Moment Predictions

Force and moment tests[49] were performed at the NASA Glenn 8- by 6-foot Wind Tunnel.[50] The simulation conditions are 1.56 Mach and 4.82 million Reynolds number per foot or 3.38 million Reynolds number for the mean aerodynamic chord. The `hvanalbada` limiter is used with the Roe flux function and SA turbulence model. The drag integration surfaces are shown in gray in Fig. 14. The red model support sting is omitted from the simulation force calculation. The wind tunnel walls are not modeled in the simulation; freestream boundary conditions are applied to the outer boundaries.

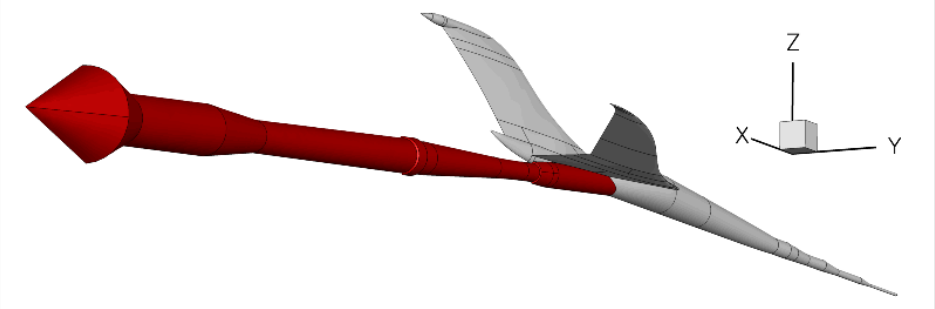

Figure 14. Gray force integration surface and red model support sting.

Three different grids are used for this simulation. They contain 2.85, 5.40, and 7.67 million nodes. The patches and sources had to be modified to produce the two finest grids.[45] Producing a family of uniformly refined unstructured grids remains an open topic. To provide an example of the typical iterative convergence for these grids, the iterative convergence at 3.917 degrees angle of attack is shown for all three grids in Fig. 15. The continuity equation is plotted with solid lines and the SA turbulence residual is plotted with dashed lines. The limiter was frozen at iteration 1,000 and a total of 3,000 iterations were performed. The flow equation residual was reduced six orders of magnitude and the turbulence model residual was reduced five orders of magnitude from its peak. The convergence rate of all three grids is very similar.

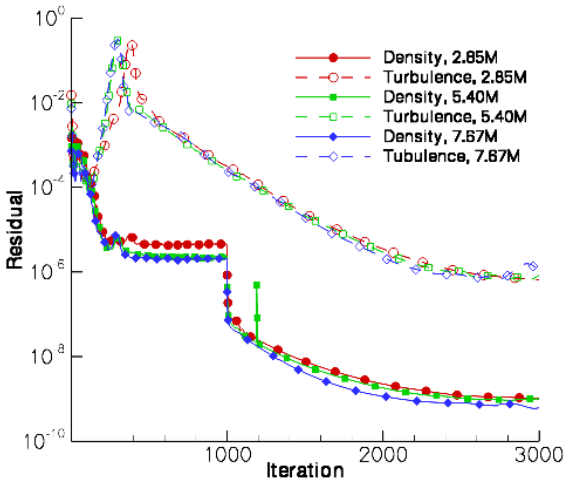

Figure 15. Convergence history at $\alpha = 3.917$ for three grid resolutions.

The longitudinal forces and moments of the model (excluding the sting and base) are shown in Fig. 16 and Fig. 17 as a function of angle of attack. Lift as a function of drag and pitching moment is shown in Fig. 18. All three grid levels are shown. The simulation was performed at the same angles of attack as the wind tunnel measurements. The slope of the predicted lift curve is higher than the measured lift curve slope, Fig. 16a. The predicted drag values are larger than the measurements for the entire angle of attack range, Fig. 16b. The slope of the predicted pitching moment is steeper than the measurements, Fig. 17. The predicted and measured pitching moments agree best near zero lift. The measured change in slope near five

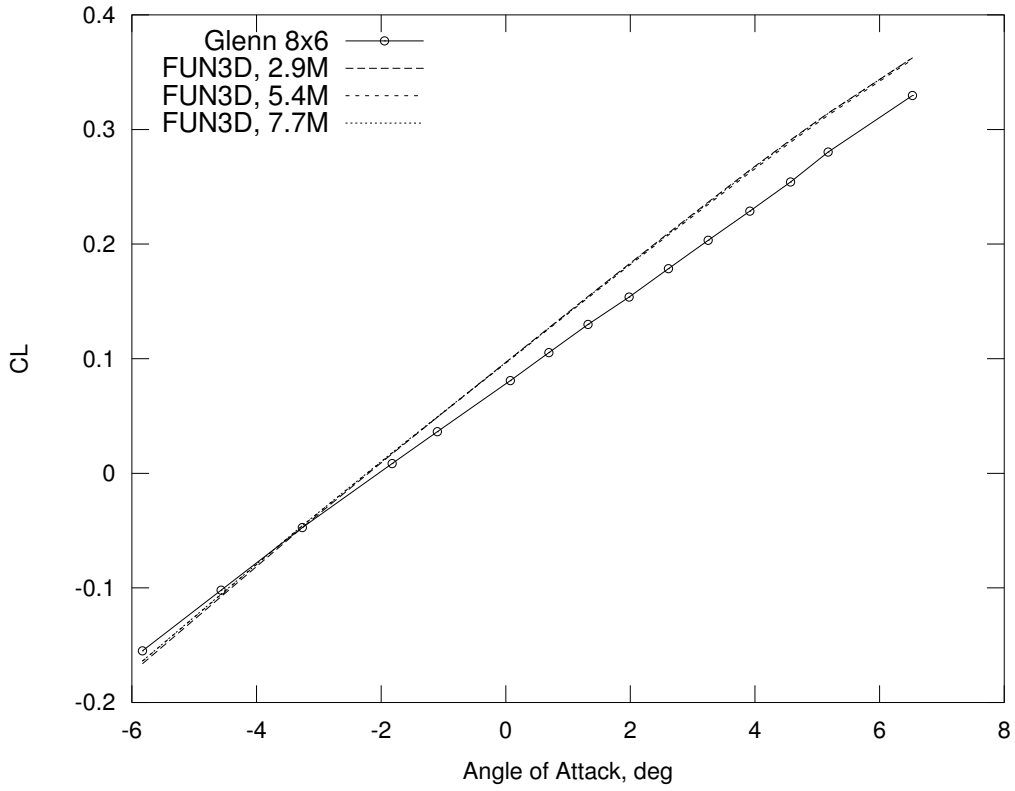

(a) Coefficient of lift.

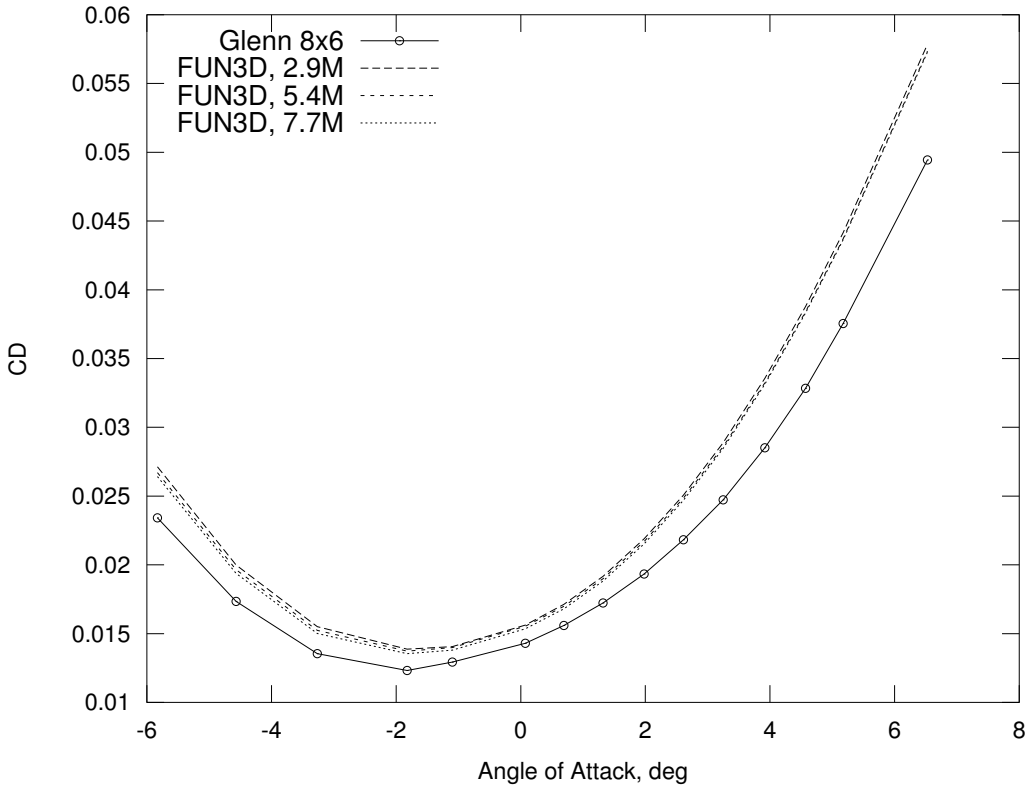

(b) Coefficient of drag.

Figure 16. Longitudinal forces as a function of angle of attack.

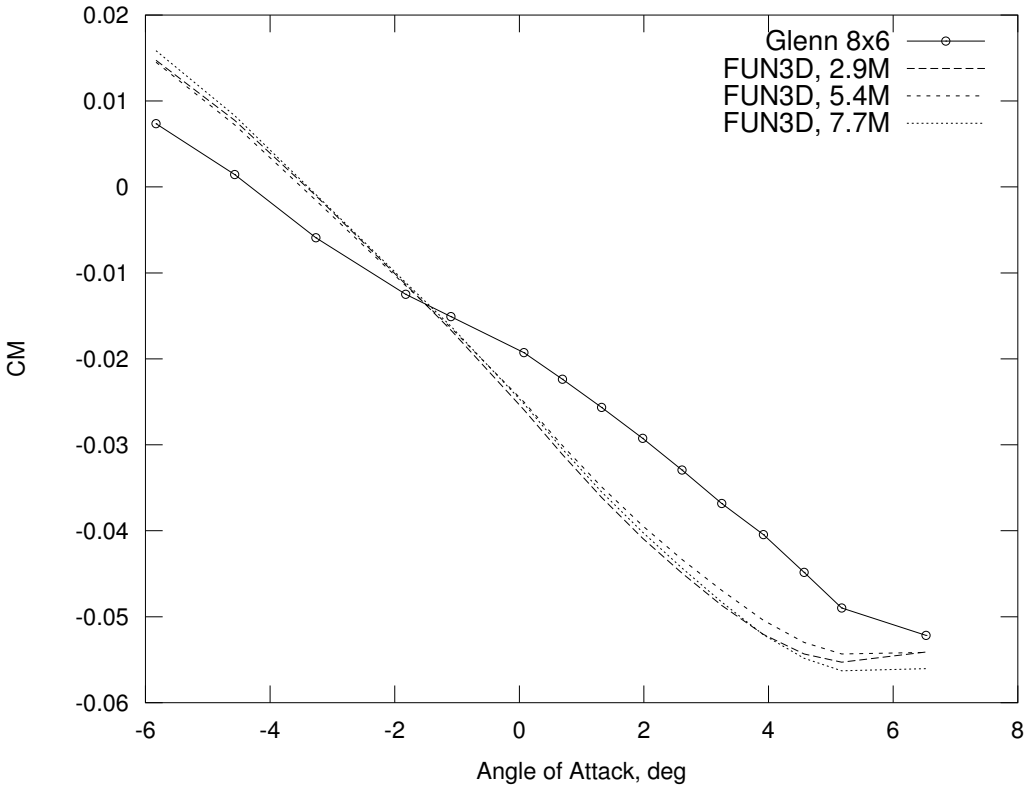

Figure 17. Coefficient of pitching moment as a function of angle of attack.

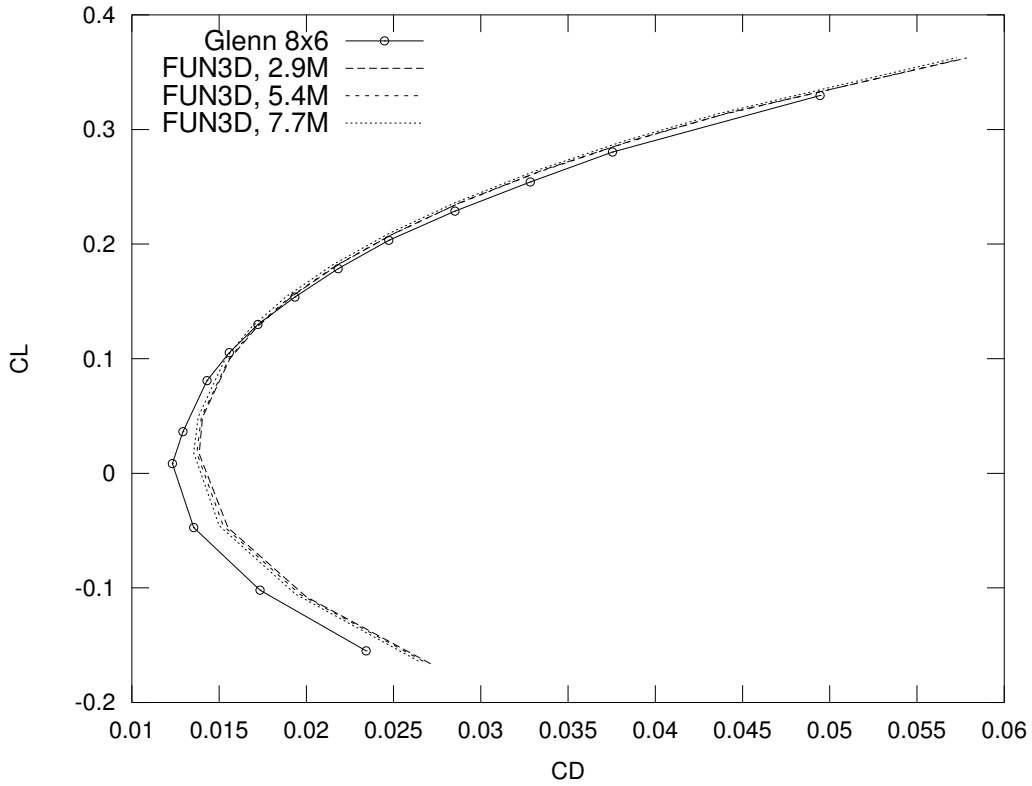

(a) Coefficient of lift as a function of drag.

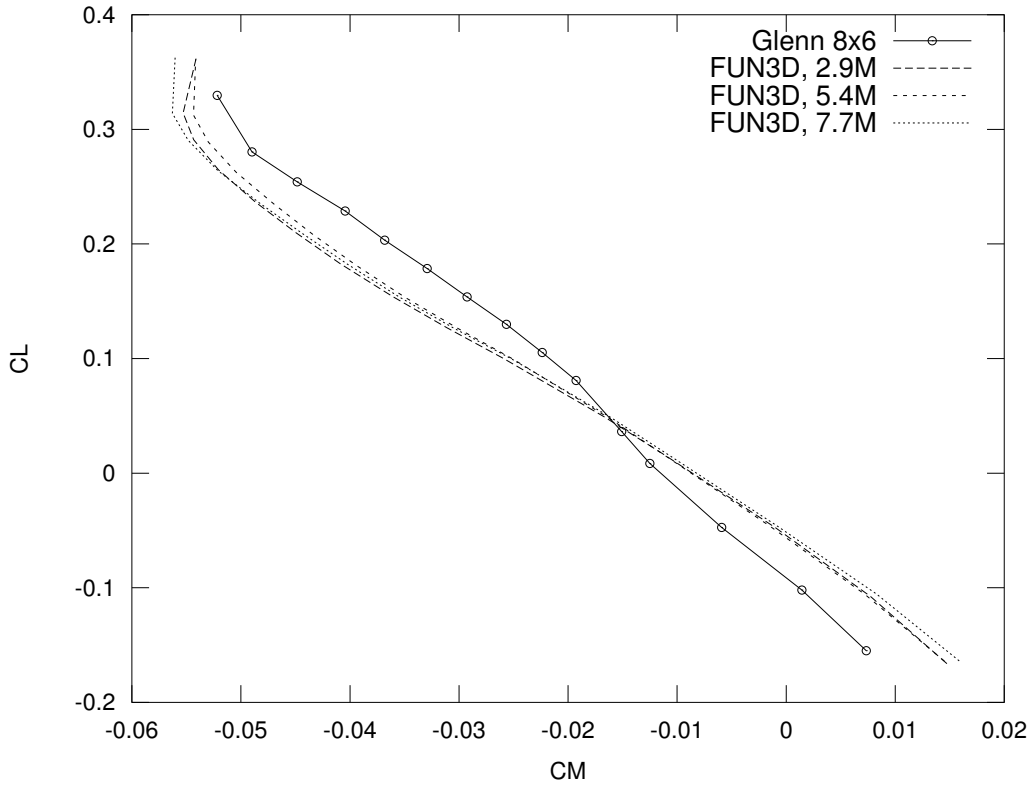

(b) Coefficient of lift as a function of pitching moment.

Figure 18. Lift as a function of drag and pitching moment.

degrees angle of attack is also seen in the simulation. The variation with grid resolution is greatest for drag at negative angles of attack and large magnitude pitching moment. The variation due to grid resolution is much smaller than the difference between the measurements and simulation.

Lift as a function of drag and pitching moment is shown in Fig. 18. The differences between the measured and predicted data in Fig. 16 collapse for positive lift, Fig. 18a. The grid sensitivity is greatest for the negative lift portion of the curve. USM3D also showed that the prediction of lift as a function of drag was better than lift or drag as a function of angle of attack.[45] USM3D[51] utilizes a cell-centered discretization, so it has approximately six times as many control volumes as node-centered FUN3D for the same grid.

VII. Conclusions

Simulations were performed to obtain off-body delta pressures, forces, and moments for the Gulfstream Low Boom Model. The off-body delta pressure predictions were compared with wind tunnel measurements of a model with a blade sting model support. The predicted forces and moments were compared to wind tunnel tests of a model with a conventional rear sting model support system. All of the simulations were performed with RANS coupled with the SA turbulence model to include the effects of a turbulent boundary layer. Off-body pressure predictions have historically been performed with Euler methods. This was the first application of a viscous output adaptive technique to predict off-body pressure of a 3D wing body configuration. The adaptation mechanics do not currently permit the modification of the grid in the lowest portion of the boundary layer.

The output adaptive approach was compared to an *a priori* grid adaptation technique that stretches and aligns the grid to the freestream Mach cone. The *a priori* adaptation method resolved small, high frequency pressure disturbances on the aircraft centerline, but was less accurate for off-centerline predictions. The output adaptive technique simultaneously targeted centerline and off-centerline portions of the signal and provided balanced predictions that were good on and off the centerline. If desired by the engineer, the centerline resolution can be increased and off-centerline resolution reduced by the tailoring the sensor location to only include the region near the centerline. An improvement to the Hessian recovery method or an output-based approach that directly determines the anisotropy may improve the output adaptive results.

One of the presented wind tunnel measurements used grit to trip the boundary layer. The grit produced measurable signature changes at the grit location that were not modeled in simulation. The application of grit also changed the aft portion of the measured signature, but it was unclear if the fully turbulent boundary layer simulations better matched the tripped or untripped case. The eddy viscosity predicted by the SA turbulence model increased dramatically with grid adaptation.

Computed lift as a function of computed drag compared very favorably with wind tunnel measurements for positive lift, but predicted lift and drag as a function of angle of attack had significant differences from the measured data. Predicted pitching moment as a function of angle of attack or lift had the same general trends, but slightly different slopes. The measured and predicted pitching moments were closest near zero lift. The forces and moments of the configuration were computed with a series of refined grids. A weak sensitivity to grid refinement was noted, but could not justify the differences in the computed and measured data. This suggests that the differences between experimental and computational results may include significant modeling errors as well as discretization errors.

Acknowledgments

Sudheer Nayani of Analytical Services & Materials, Inc. provided the series of refined grids for the force and moment study and the initial viscous grid for the sonic boom adaptation study. NASA Fundamental Aeronautics Program Supersonics Project provided support for this work.

References

[1]Plotkin, K. J., "State of the Art of Sonic Boom Modeling," *The Journal of the Acoustical Society of America*, Vol. 111, No. 1, Jan. 2002, pp. 530–536.

[2]Ozcer, I. A., *Sonic Boom Prediction Using Euler/Full-Potential Methodology*, Master's thesis, Old Dominion University, Dec. 2005.

[3]Park, M. A., *Anisotropic Output-Based Adaptation with Tetrahedral Cut Cells for Compressible Flows*, Ph.D. thesis, Massachusetts Institute of Technology, Sept. 2008.

[4]Campbell, R., Carter, M., Deere, K., and Waithe, K. A., "Efficient Unstructured Grid Adaptation Methods for Sonic Boom Prediction," AIAA Paper 2008–7327, 2008.

[5]Laflin, K. R., Klausmeyer, S. M., and Chaffin, M., "A Hybrid Computational Fluid Dynamics Procedure for Sonic Boom Prediction," AIAA Paper 2006–3168, 2006.

[6]Kandil, O. and Ozcer, I. A., "Sonic Boom Computations for Double-Cone Configuration using CFL3D, FUN3D and Full-Potential Codes," AIAA Paper 2006–414, 2006.

[7]Waithe, K. A., "Application of USM3D for Sonic Boom Prediction by Utilizing a Hybrid Procedure," AIAA Paper 2008–129, 2008.

[8]Alauzet, F. and Loseille, A., "High-Order Sonic Boom Modeling Based on Adaptive Methods," *Journal of Computational Physics*, Vol. 229, No. 3, 2010, pp. 561–593.

[9]Ozcer, I. A. and Kandil, O., "FUN3D / OptiGRID Coupling for Unstructured Grid Adaptation for Sonic Boom Problems," AIAA Paper 2008–61, 2008.

[10]Fidkowski, K. J. and Darmofal, D. L., "Output-Based Adaptive Meshing Using Triangular Cut Cells," Technical Report ACDL TR-06-2, Aerospace Computational Design Laboratory, Department of Aeronautics and Astronautics, Massachusetts Institute of Technology, 2006.

[11]Barter, G. E., *Shock Capturing with PDE-Based Artificial Viscosity for an Adaptive, Higher-Order Discontinuous Galerkin Finite Element Method*, Ph.D. thesis, Massachusetts Institute of Technology, 2008.

[12]Nemec, M., Aftosmis, M. J., and Wintzer, M., "Adjoint-Based Adaptive Mesh Refinement for Complex Geometries," AIAA Paper 2008-725, 2008.

[13]Jones, W. T., Nielsen, E. J., and Park, M. A., "Validation of 3D Adjoint Based Error Estimation and Mesh Adaptation for Sonic Boom Prediction," AIAA Paper 2006–1150, 2006.

[14]Park, M. A. and Darmofal, D., "Validation of an Output-Adaptive, Tetrahedral Cut-Cell Method for Sonic Boom Prediction," *AIAA Journal*, Vol. 48, No. 9, Sept. 2010, pp. 1928–1945.

[15]Alauzet, F., Dervieux, A., and Loseille, A., "Fully Anisotropic Goal-Oriented Mesh Adaptation for 3D Steady Euler Equations," *Journal of Computational Physics*, Vol. 229, No. 8, 2010, pp. 2866–2897.

[16]Meredith, K., Dahlin, J., Graham, D., Malone, M., Haering, E., Page, J., and Plotkin, K., "Computational Fluid Dynamics Comparison and Flight Test Measurement of F-5E Off-Body Pressures," AIAA Paper 2005–6, 2005.

[17]Morgenstern, J. M., "Wind Tunnel Testing of a Sonic Boom Minimized Tail-Braced Wing Transport Configuration," AIAA Paper 2004–4536, 2004.

[18]Furukawa, T., Makino, Y., Noguchi, M., and Ito, T., "Supporting System Study of Wind-Tunnel Models for Validation of Aft-Sonic-Boom Shaping Design," AIAA Paper 2008–6596, 2008.

[19]Carlson, H. W. and Morris, O. A., "Wind-Tunnel Sonic-Boom Testing Techniques," *AIAA Journal of Aircraft*, Vol. 4, No. 3, 1967, pp. 245–249.

[20]Park, M. A. and Carlson, J.-R., "Turbulent Output-Based Anisotropic Adaptation," AIAA Paper 2010–168, 2010.

[21]Seebass, R., "Sonic Boom Theory," *AIAA Journal of Aircraft*, Vol. 6, No. 3, May–June 1969, pp. 177–184.

[22]Anderson, W. K. and Bonhaus, D. L., "An Implicit Upwind Algorithm for Computing Turbulent Flows on Unstructured Grids," *Computers and Fluids*, Vol. 23, No. 1, 1994, pp. 1–22.

[23]Roe, P. L., "Approximate Riemann Solvers, Parameter Vectors, and Difference Schemes," *Journal of Computational Physics*, Vol. 43, 1981, pp. 357–372.

[24]van Leer, B., "Flux-Vector Splitting for the Euler Equations," *Lecture Notes in Physics*, Vol. 170, 1982, pp. 507–512.

[25]Barth, T. J. and Jespersen, D. C., "The Design and Application of Upwind Schemes on Unstructured Meshes," AIAA Paper 89–366, 1989.

[26]van Albada, G. D., van Leer, B., and Roberts, Jr., W. W., "A Comparative Study of Computational Methods in Cosmic Gas Dynamics," *Astronomy and Astrophysics*, Vol. 108, 1982, pp. 76–84.

[27]Venkatakrishnan, V., "Convergence to Steady State Solutions of the Euler Equations on Unstructured Grids with Limiters," *Journal of Computational Physics*, Vol. 118, No. 1, 1995, pp. 120–130.

[28]Nielsen, E. J., Lu, J., Park, M. A., and Darmofal, D. L., "An Implicit, Exact Dual Adjoint Solution Method for Turbulent Flows on Unstructured Grids," *Computers and Fluids*, Vol. 33, No. 9, 2004, pp. 1131–1155.

[29]Spalart, P. R. and Allmaras, S. R., "A One-Equation Turbulence Model for Aerodynamic Flows," *La Recherche Aerospatiale*, Vol. 1, No. 1, 1994, pp. 5–21.

[30]Nielsen, E. J. and Anderson, W. K., "Recent Improvements in Aerodynamic Design Optimization on Unstructured Meshes," *AIAA Journal*, Vol. 40, No. 6, 2002, pp. 1155–1163.

[31]Nielsen, E. J., *Aerodynamic Design Sensitivities on an Unstructured Mesh Using the Navier-Stokes Equations and a Discrete Adjoint Formulation*, Ph.D. thesis, Virginia Polytechnic Institute and State University, 1998.

[32]Eisenstat, S. C., Elman, H. C., and Schultz, M. H., "Variational Iterative Methods for Nonsymmetric Systems of Linear Equations," *SIAM Journal on Numerical Analysis*, Vol. 2, April 1983, pp. 345–357.

[33]Venditti, D. A., *Grid Adaptation for Functional Outputs of Compressible Flow Simulations*, Ph.D. thesis, Massachusetts Institute of Technology, 2002.

[34]Park, M. A., "Three–Dimensional Turbulent RANS Adjoint–Based Error Correction," AIAA Paper 2003–3849, 2003.

[35]Lee-Rausch, E. M., Park, M. A., Jones, W. T., Hammond, D. P., and Nielsen, E. J., "Application of a Parallel Adjoint-Based Error Estimation and Anisotropic Grid Adaptation for Three-Dimensional Aerospace Configurations," AIAA Paper 2005–4842, 2005.

[36]Park, M. A., Lee-Rausch, E. M., and Rumsey, C. L., "FUN3D and CFL3D Computations for the First High Lift Prediction Workshop," AIAA Paper 2011–936, 2011.

[37]Park, M. A. and Darmofal, D., "Parallel Anisotropic Tetrahedral Adaptation," AIAA Paper 2008–917, 2008.

[38]Diskin, B., Thomas, J. L., Nielsen, E. J., Nishikawa, H., and White, J. A., "Comparison of Node-Centered and Cell-Centered Unstructured Finite-Volume Discretizations: Viscous Fluxes," *AIAA Journal*, Vol. 48, No. 7, July 2010, pp. 1326–1338.

[39]Andren, J. and Park, M. A., "Output Based Grid Adaptation for Viscous Flow," 18th International Meshing Roundtable Research Notes, Sandia National Lab, Oct. 2009, pp. 1–5.

[40]Howe, D. C., Simmons, III, F., and Freund, D., "Development of the Gulfstream Quiet Spike for Sonic Boom Minimization," AIAA Paper 2008–124, 2008.

[41]Wayman, T., Howe, D. C., Waithe, K. A., Bangert, L., and Wilcox, F., "Near Field Acoustic Test on a Low Boom Configuration in Langley's 4 x 4 Wind Tunnel," 29th AIAA Applied Aerodynamics Conference, American Institute of Aeronautics and Astronautics, Reston, VA (submitted for publication).

[42]Jackson, Jr., C. M., Corlett, W. A., and Monta, W. J., *Description and Calibration of the Langley Unitary Plan Wind Tunnel*, NASA TP 1905, Nov. 1981.

[43]Wassum, D. L. and Hyman, Jr., C. E., *Procedures and Requirements for Testing in the Langley Research Center Unitary Plan Wind Tunnel*, NASA TM 100529, Feb. 1988.

[44]Waithe, K. A., "Design of a Wind Tunnel Mount for Low Boom Test," 29th AIAA Applied Aerodynamics Conference, American Institute of Aeronautics and Astronautics, Reston, VA (submitted for publication).

[45]Carter, M. B., Campbell, R. L., and Nayani, S. N., "USM3D Analysis of Low Boom Configuration," 29th AIAA Applied Aerodynamics Conference, American Institute of Aeronautics and Astronautics, Reston, VA (submitted for publication).

[46]Oliver, T. A. and Darmofal, D. L., "Impact of Turbulence Model Irregularity on High-Order Discretizations," AIAA Paper 2009–953, 2009.

[47]Mack, R. J., *Method for Standardizing Sonic-Boom Model Pressure Signatures Measured at Several Wind-Tunnel Facilities*, NASA/TM-2006-214854, 2007.

[48]Elmiligui, A., Cliff, S. E., Aftosmis, M. J., Nemec, M., Parlette, E., Wilcox, F., and Bangert, L., "Sonic Boom Computations for a Mach 1.6 Cruise Low Boom Configuraion and Comparisons with Wind Tunnel Data," 29th AIAA Applied Aerodynamics Conference, American Institute of Aeronautics and Astronautics, Reston, VA (submitted for publication).

[49]Wayman, T., Hicks, G., and Merret, J., "Force and Moment Test on a Low Boom Configuration in Glenn's 8 x 6 Tunnel," 29th AIAA Applied Aerodynamics Conference, American Institute of Aeronautics and Astronautics, Reston, VA (submitted for publication).

[50]Soeder, R. H., *NASA Lewis 8- By 6-Foot Supersonic Wind Tunnel User Manual*, NASA TM–105771, Feb. 1993.

[51]Frink, N. T. and Pirzadeh, S. Z., "Tetrahedral Finite Volume Solutions to the Navier Stokes Equations on Complex Configurations," *International Journal for Numerical Methods in Fluids*, Vol. 31, No. 1, 1999, pp. 175–187.